Manipulating the Corrosion Resistance of SnO2 Aerogels Trough Doping for Efficient and Durable Oxygen Evolution Reaction Electrocatalysis in Acidic Media

Sofyane Abbou, Raphaël Chattot, V. Martin, Fabien Claudel, Lluís Solà-Hernández, Christian Beauger, Laetitia Dubau, Frédéric Maillard

Manipulating the Corrosion Resistance of SnO_2 Aerogels Trough Doping for Efficient and Durable Oxygen Evolution Reaction Electrocatalysis in Acidic Media

Sofyane Abbou, [γ,†] *Raphaël Chattot,* [γ,†] *Vincent Martin,* [†] *Fabien Claudel,* [†] *Lluís Solà-Hernandez,* [‡] *Christian Beauger,* [‡] *Laetitia Dubau,* [†] *Frédéric Maillard* [†,*]

† Univ. Grenoble Alpes, Univ. Savoie Mont Blanc, CNRS, Grenoble INP, LEPMI, 38000 Grenoble, France

‡ MINES ParisTech, PSL University, Centre procédés, énergies renouvelables et systèmes énergétiques (PERSEE), CS 10207 rue Claude Daunesse, F-06904 Sophia Antipolis Cedex, France

ABSTRACT

Implementing iridium oxide (IrO_x) nanocatalysts can be a major breakthrough for oxygen evolution reaction (OER), the limiting reaction in polymer electrolyte membrane water electrolyser devices. However, this strategy requires developing a support that is electronically conductive, is stable in OER conditions, and features a large specific surface area and a porosity adapted to gas-liquid flows. To address these challenges, we synthesized IrO_x nanoparticles, supported them onto doped SnO_2 aerogels (IrO_x/doped SnO_2), and assessed their electrocatalytic activity towards the OER and their resistance to corrosion in acidic media by means of a flow cell connected to an inductively-coupled mass spectrometer (FC-ICP-MS). The FC-ICP-MS results show that the long-term OER activity of IrO_x/doped SnO_2 aerogels is controlled by the resistance to corrosion of the doping element, and by its concentration in the host SnO_2 matrix. In particular, we provide quantitative evidence that Sb-doped SnO_2 type supports continuously dissolve while Ta-doped or Nb-doped SnO_2 supports with appropriate doping concentrations are stable under acidic OER conditions. These results shed fundamental light on the complex

equilibrium existing between SnO_2 and the doping element oxide. They also open a reliable path to develop highly active and robust IrO_x nanocatalysts for OER in acidic media.

KEYWORDS: Proton-exchange membrane water electrolysers; oxygen evolution reaction; iridium oxide; doped tin oxide; *in situ* inductively coupled plasma mass spectrometry.

INTRODUCTION

The increasing demand of energy and the necessity to decrease carbon dioxide (CO_2) emissions currently boost the search for zero-carbon emitting alternative energy sources. Technologies based on molecular hydrogen (H_2) have long been identified as the most promising solution to decarbonise power, buildings, industry and transportation segments. However, because the major part of H_2 is currently produced via natural gas steam reforming, oil reforming and coal gasification, the problem of CO_2 emissions persists. The electrochemical splitting of water, leading to evolution of molecular H_2 at the cathode and molecular oxygen (O_2) generation at the anode, is a sustainable way to promote the development of this energy vector [1].

Alkaline water electrolysers (AWE) industrially produce the major part of electrochemical H_2. These systems use electrodes based on abundant and low cost materials (iron or nickel steel and nickel for hydrogen evolution reaction (HER) and oxygen evolution reaction (OER), respectively), and highly concentrated alkaline aqueous

solution (typically 20-30 wt. % potassium hydroxide [2-4]) as an electrolyte. However, AWEs are limited in performance to current densities below 0.5 A cm^{-2} (limited electrolyte conductivity and risk of H_2 and O_2 mixing at higher currents), their start-up is slow, and the liquid electrolyte may be expelled from the device during sudden current changes ("champagne effect"). [5-6] These characteristics prevent using dynamic current transients such as those required to store electrical energy coming from renewable energy sources. [6] In contrast, the ability of polymer electrolyte membrane water electrolysers (PEMWE) to operate in a dynamic manner, to sustain current densities up to 3 A cm^{-2}, and to produce pressurized H_2 (up to 100 bars) makes these devices most suitable to store the energy collected from wind and solar sources. Nevertheless, the acidic electrolyte requires usage of large quantities of platinum-group metals (PGM), typically between 0.3 and 1 mg_{Pt} cm^{-2} and between 2 and 4 mg_{Ir} cm^{-2} at the cathode and anode, respectively [7]. Although the contribution of electrocatalysts' cost to the total cost of a PEMWE currently represents only 6 %, [5, 8-10] a reduction of the PGM loading will in any case contribute to limit the pressure on these two rare metals in the future. Moreover, any improvement in PEMWE efficiency will help diminishing the number of cells composing the stacks as well as

decreasing the associated materials cost (bipolar plates, membrane, porous transport layers etc.).

Different strategies have been implemented to overcome the PGM content issue in PEMWEs. Recently, Bernt *et al.* reported the possibility to decrease the Pt loading at the cathode from 0.3 to 0.025 mg_{Pt} cm^{-2} without any adverse effect on the initial PEMWE performance [8]. However, the most difficult consists in reducing the Ir loading due to the sluggish kinetics of the OER. A direct reduction has been studied by the groups of Millet and Gasteiger. Rozain *et al.* [11-12] reported a decrease of the PEMWE performance for IrO_2 loading below 0.7 mg cm^{-2} that they ascribed to poor IrO_2 utilization. Similarly, Bernt *et al.* [8] observed that the PEMWE performance decreases drastically for Ir loading below 0.5 mg cm^{-2} (*ca.* 2 µm thick anodes), due to the inhomogeneous and non-contiguous character of the catalytic layer. Mixing IrO_2 with one metal oxide (IrO_2 + SnO_2 [13-16], IrO_2 + Ta_2O_5 [17-18], IrO_2 + Nb_2O_5 [19], IrO_2 + TiO_2 [20-21], IrO_2 + Sb_2O_5 [22]) or more (*e.g.* SnO_2-IrO_2-Ta_2O_5 [23]) was investigated a decade ago but revealed a dead-end because it causes a drop in electronic conductivity and associated increase of the PEMWE cell voltage. Based

on these studies, a > 10-fold reduction of the Ir loading will be hard to achieve without a breakthrough in the nature of the OER materials.

Supporting iridium oxide (IrO_x) nanoparticles (NPs) on a metal oxide is an attractive strategy to reach this ambitious goal. However, it requires developing a support, which (i) possesses an opened and interconnected structure compatible with facile water/O_2 transport and ionomer insertion, (ii) features a large specific surface area to maximize the distribution of the IrO_x NPs while prevents their agglomeration/aggregation, (iii) possesses high electronic conductivity, and (iv) is corrosion resistant. While the first and second requirements can be met by fine tuning the synthesis parameters of the metal oxide support, simultaneously meeting the criteria (iii) and (iv) is highly challenging. Indeed, TiO_2, Nb_2O_3, MoO_3, SnO_2, Sb_2O_5 and Ta_2O_5 fulfil the stability criterion in polymer electrolyte membrane fuel cell (PEMFC) cathode conditions but studies focusing on their resistance to corrosion in PEMWE anode operating conditions are scarce. [24] Moreover, since most of the metal oxides are semiconductors, doping with hypovalent or hypervalent ions is a pre-requisite to high electron conductivity, [25] and any variation in the doping

concentration leads to severe ohmic losses. In this frame, Fabbri *et al.* [26] have shown that the loss of antimony (Sb) from Sb-doped tin dioxide (SnO_2, ATO), one of the most used metal oxides, leads to the formation of Sb-poor shell covering a core with the same Sb content than the virgin ATO but depreciated electronic conductivity. The authors also reported that the extent of Sb dissolution is emphasized during alternation of reducing (0.05 V *vs*. the reversible hydrogen electrode, RHE) and oxidizing (1.6 V *vs*. RHE) potential. Importantly, Cognard *et al*. [27-28] showed that dissolved Sb^{z+} ions (z = 3 or 5) redeposit onto the surface of Pt NPs in PEMFC cathode conditions, eventually poisoning their activity towards the oxygen reduction reaction. In experimental conditions simulating a PEMWE anode environment, Geiger *et al.* [29] provided evidence that both indium (In) and Sb atoms leach out from In-doped tin oxide (ITO) and ATO, respectively during potential sweeps between -0.6 and 2.0 V *vs*. RHE. Massive Sn dissolution was also evidenced during cathodic potential sweeps, in agreement with the early findings of Fabbri *et al.* [26]. The stability domains of Sn and Sb were thus empirically defined as: -0.29 V < E < 1.45 V *vs*. RHE and 0.36 V < E < 1.1 V *vs*. RHE, respectively. By combining identical-location transmission electron microscopy and energy-dispersive X-ray

spectroscopy (IL-TEM and X-EDS, respectively), Claudel *et al.* [30] recently evidenced that IrO_x NPs supported onto ATO survive potential cycling between 1.2 and 1.6 V *vs*. RHE but become electrically-disconnected from the support. Hence, the quest of stable, pentavalent doping elements for metal oxide-supported IrO_x nanocatalysts is still ongoing.

Here, using a flow cell connected to an inductively-coupled mass spectrometer (FC-ICP-MS), we demonstrate that the stability of doped SnO_2 aerogel supports in acidic OER conditions is in fact limited by the susceptibility of the oxide layers forming to (electro)chemically dissolve. To this goal, we synthesized a library of doped SnO_2 aerogel supports featuring rutile structure, high specific surface area, and morphology adapted to the specifications of PEMWE anode, and functionalized them with IrO_x NPs *ca*. 1.4 nm in size using a highly reproducible method. The FC-ICP-MS results not only make it possible to shed light on the degradation mechanisms of these nanocatalysts (detachment of IrO_x NPs assisted by doped SnO_2 corrosion, anodic/cathodic dissolution of IrO_x) but also revealed that IrO_x NPs deposited onto tantalum-doped aerogel (IrO_x/TaTO) with appropriate doping concentration combine the OER activity and stability requirements.

RESULTS AND DISCUSSION

Synthesis and Characterization of IrO_x/doped SnO_2 Aerogels Supports

A scheme of the synthesis of the supported IrO_x NPs is presented in **Figure 1**. In brief, doped SnO_2 aerogels were first synthesized via a sol-gel process in which a solution containing Sn and the doping element precursors (Sb, Nb or Ta) was progressively transformed into a gel before being dried and ultimately calcined under air at T = 600°C (see Supporting Information). In what follows, these aerogels are referred to as MTO-X, where M is the doping element (M = Sb (A), Ta (Ta), Nb (N)) and X is the effective doping concentration [X = M/(M+Sn)] determined from local X-EDS analyses. IrO_x NPs with narrow particle size distribution (~1.4 ± 0.3 nm, see in **Figure S1**) were obtained via a modified polyol route, [30] and further deposited onto the various MTO aerogels investigated. This strategy ensured a straightforward comparison of their catalytic performance towards the OER and their resistance to degradation. A nominal IrO_x weight fraction (wt. %) of 20 wt. % was targeted, however the effective Ir wt. % (measured by

ICP-MS after microwave oven-assisted digestion of the samples in *aqua regia*, see Supporting Information) was dependent on the morphological characteristics of the aerogels. The Ir wt. % values (displayed in **Table 1** and **Table S1)** were comprised between 16.5 and 18.0 wt. % for IrO_x/ATO-10, IrO_x/NTO-10, IrO_x/TaTO-5 and IrO_x/TaTO-18 but decreased down to 10.7 wt. % for IrO_x/TaTO-2.5, most likely due to its smaller specific surface area (*ca*. 34 m^2 g^{-1}) compared to the former ones (*ca*. 40-80 m^2 g^{-1}).

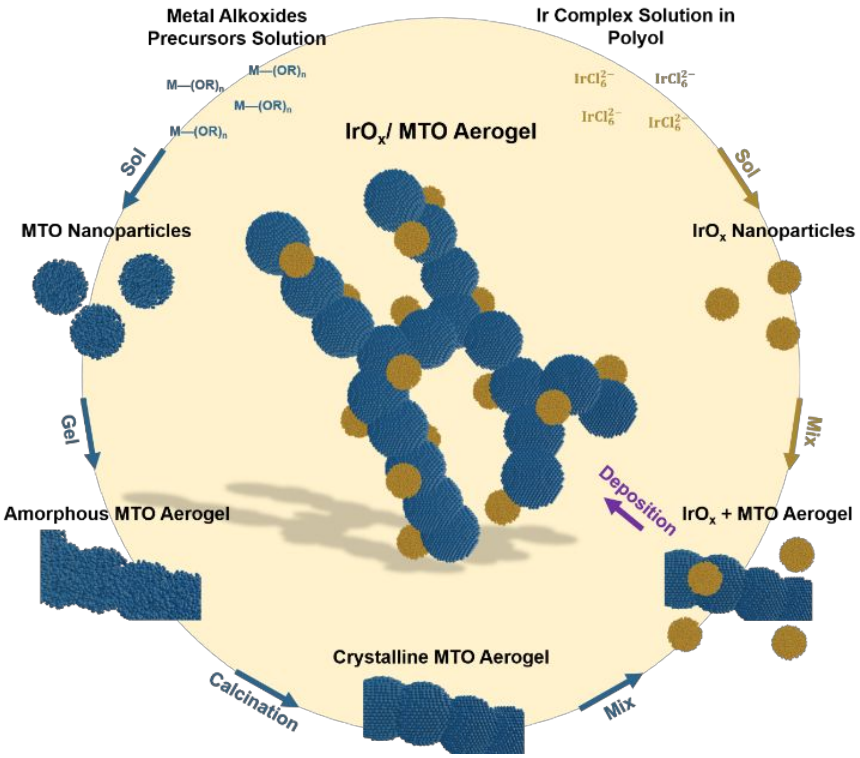

Figure 1. Scheme of the synthesis of IrO_x nanoparticles supported onto doped SnO_2 aerogels. The SnO_2 aerogels were obtained via a sol-gel process and the IrO_x nanoparticles via an independent polyol route. This strategy ensured a straightforward comparison of their catalytic performance towards the OER and their resistance to degradation.

Transmission electron microscopy (TEM) images of the synthesized nanocatalysts and X-ray diffractograms displayed in **Figure 2** show that all SnO_2-based aerogels are crystalline and feature 3D close-packed monolithic morphology composed of particles connected to each other. Their specific surface area and bulk chemical composition both depend on the sol gel parameters and on the chemical nature and concentration of the doping elements (**Table 1**, **Table S1** and **Figure S2**).

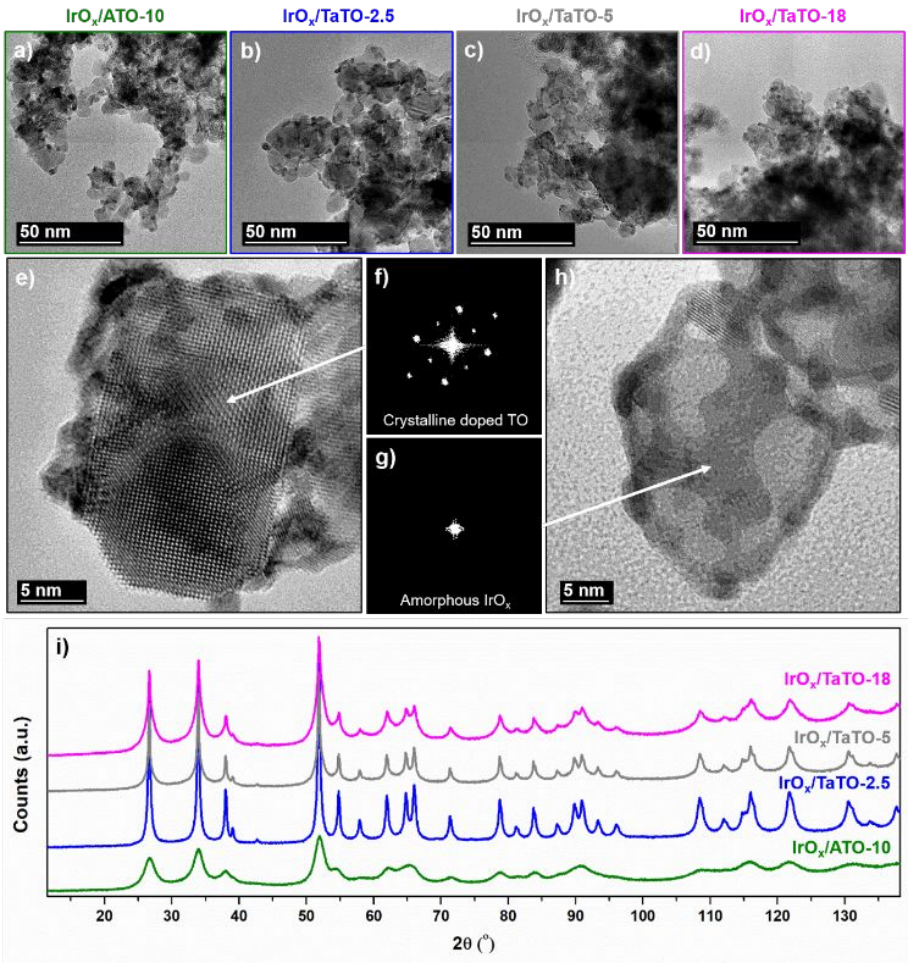

Figure 2. Transmission electron microscopy, electron diffraction images and X-ray diffractograms of IrO_x nanoparticles supported on: a) ATO-10 aerogel, b) TaTO-2.5 aerogel, c) TaTO-5 aerogel and d) TaTO-18 aerogel. e-h) High resolution transmission electron microscopy typical images with associated fast Fourier transformation showing the crystalline structure of the doped SnO_2 aerogel supports (here TaTO-1) and the

amorphous structure of the IrO_x nanoparticles. All peaks from the 8.05 keV X-ray diffraction patterns in i) are associated to cassiterite SnO_2 (space group: $P4_2/mmm$).

Table 1. Structural and substructural properties of the doped SnO_2-supported catalysts. The doping concentration ($M/(M+Sn)$ where M = Sb or Ta) was determined from X-EDS measurements, the aerogel particle size from SEM measurements, the aerogel crystallite size and lattice constants from XRD measurements, the aerogel specific surface area from nitrogen sorption (BET) measurements, the aerogel conductivity from dc-measurements and the Ir wt. % from inductively coupled plasma mass spectrometry measurements.

Catalysts	IrO_x/ATO-10	IrO_x/TaTO-2.5	IrO_x/TaTO-5	IrO_x/TaTO-18
Sb, Nb or Ta doping [at.%]	11.0	2.4	4.8	17.9
Aerogel particle size [nm]	13.8	18.5	15.8	15.7
Aerogel cryst. size [nm]	4.1	17.0	14.1	6.0
Aerogel lattice constants *a/c* [Å]	4.72/3.18	4.74/3.18	4.74/3.18	4.74/3.19

Aerogel specific surface area [m^2 g^{-1}]	83.5	34.1	41.8	78.9
Aerogel conductivity [S cm^{-1}]	8 x 10^{-1}	3.2 x 10^{-3}	2.1 x 10^{-3}	< 1 x 10^{-3}
Ir [wt.%]	17.0	10.7	17.8	17.1

X-ray diffractograms of the catalysts powders (**Figure 2i**) revealed the single-phase, cassiterite-type structure of the various supports but no signal from the IrO_x NPs, thus attesting their amorphous structure. The lattice constants for the TaTO samples were close to those of bare SnO_2 (TO) (a = 4.737 Å and c = 3.185 Å) due to the close proximity of the radius of $Sn^{4+}$and Ta^{5+} ions (69 and 64 pm, respectively) [31]. Slightly smaller lattice constants were observed for the ATO sample, in agreement with the much smaller radius (60 pm) of Sb^{5+} ions compared to the host Sn^{4+} ions [31]. Interestingly, while the various MTOs exhibited similar aerogel particle sizes from scanning electron microscopy (SEM) images analysis (13-18 nm), the coherent domain sizes estimated from the X-ray diffraction (XRD) line broadening suggest that both the nature and concentration of the doping element influence the crystallinity of the TO aerogel. The degree of crystallinity

was enhanced for Ta doping compared to Sb (coherent domain size close to the particle size), but depreciated at high doping concentration, in line with literature [28, 32-35].

The dc-conductivity measurements revealed that doping increased the electronic conductivity from 2 × 10^{-5} S cm^{-1} for TO to a maximal value of 0.8 S cm^{-1} for ATO-10, passing through intermediate values close to 10^{-3} S cm^{-1} for TaTOs and NTO-10 (see **Table S1**). These electronic conductivity values are smaller than those reported in literature for thin films or chain-like aggregated TO powders doped with Sb, Nb, or Ta. [33, 36-38] The main reason for this is necking between the primary particles as revealed by Senoo *et al.* [36] using the "Necking Index" (the ratio of the specific surface area determined according to the Brunauer-Emmett-Teller model to that estimated from X-ray diffractograms assuming spherical and isolated MTO crystallites). These authors reported that (i) the apparent electronic conductivity of MTO supports increases with decreasing the necking index values, (ii) MTO supports featuring aggregated structure (grains connected by large phase boundaries) are better conducting electrons than agglomerated structures in which grains are connected by a point contact.

Electrochemical Characterization of the IrO_x/doped SnO_2 Aerogel Supports

Figure 3a displays the base cyclic voltammograms (CVs) recorded on the synthesized nanocatalysts, and on a commercial unsupported IrO_2 powder from Alfa Aesar after electrochemical conditioning. IrO_x NPs were also deposited on a Vulcan XC72 support (IrO_x/C), as a reference material (more information about IrO_x/C and additional reference materials can be found in **Table S1** of the Supporting Information). Whatever the support, redox peaks were observed at *ca*. 0.97/0.93 V *vs*. RHE (positive-and negative-going potential sweep, respectively), and ascribed to the Ir(III)/Ir(IV) redox transition (the presence of which was confirmed by X-ray photoelectron spectroscopy (XPS), see **Figure S3**). Note however that, based on the linear dependence of these peak potentials with pH, Kuo *et al.* [39] suggested that these peaks may be ascribed to the transition between surface adsorbed hydroxyl and oxygen. The absence of electrical charge associated with the underpotential deposition of H was another evidence that a stable oxide layer had formed after the electrochemical conditioning stage [30, 40]. The Ir mass-normalized Ohmic drop corrected OER polarization curves measured on the different supported

nanocatalysts were nearly superimposed (**Figure 3b**), and so were the OER mass activities determined at 1.51 V *vs.* RHE and 1.60 *vs.* RHE (**Figure 3c** and **Figure 3d**).

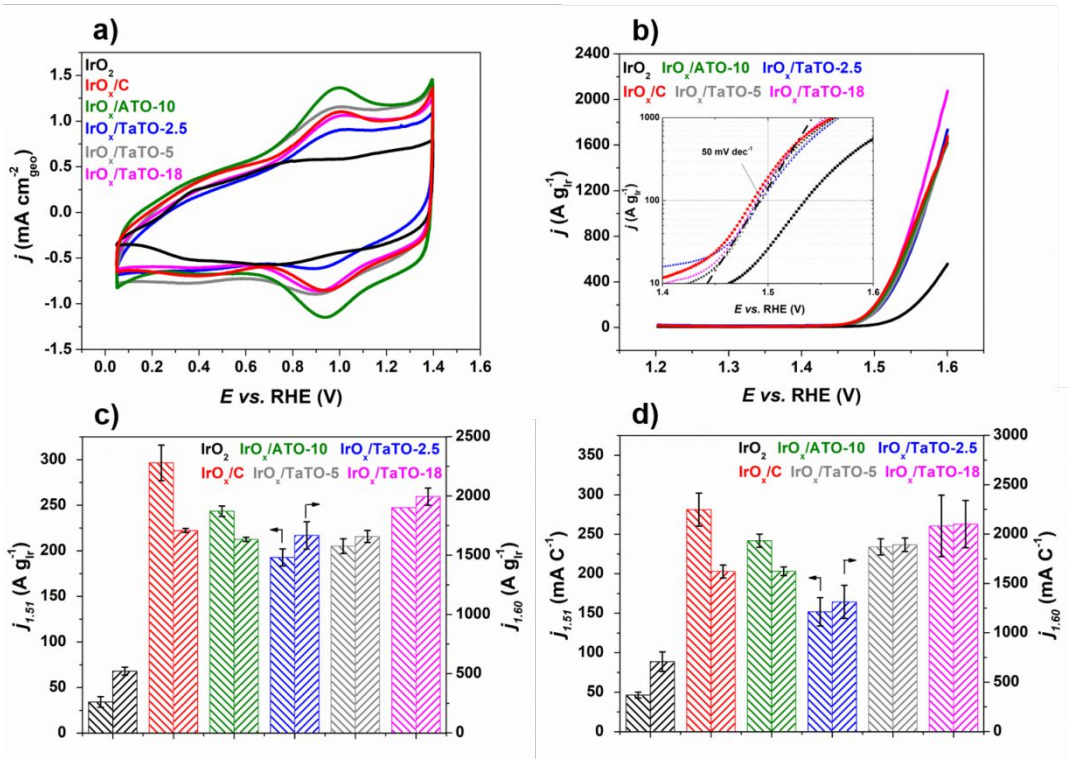

Figure 3. Electrochemical characterization and OER activity of the various catalysts investigated in this study. a) base cyclic voltammograms recorded at 50 mV s^{-1}, b) OER linear sweep voltammograms recorded at 5 mV s^{-1} with associated Tafel slopes in insert, c) Ir mass-normalized OER activity at 1.51 and 1.60 V *vs*. RHE and d) charge-normalized OER activity at 1.51 V *vs*. RHE and 1.60 V *vs*. RHE. The charge in c) was calculated by integration of the base voltammograms in a) during the anodic potential sweep in the

potential region 0.4 – 1.4 V *vs*. RHE. All curves were recorded in 0.05 M H_2SO_4 at T = 25 ºC.

For all materials, we measured OER mass activities approaching 250 A g_{Ir}^{-1} at 1.51 V *vs.* RHE (η = 280 mV), and exceeding those of the commercial IrO_2 catalyst (at least 5 times), and those of IrO_2 particles supported onto ATO reported by Lettenmeier *et al*. [41], Alia *et al.* [42] and Böhm *et al.* [43]. The synthesized materials also outperformed slightly larger IrO_x particles supported onto similar doped SnO_2 supports, [44] thus highlighting the benefits of reducing the IrO_x particle size. Strikingly, the smaller electronic conductivity of TaTO aerogel supports compared to bare ATO-10 (300-fold decrease, see **Table 1**) did not result in depreciated OER activity. This confirms that the presence of IrO_x NPs onto the aerogels surface helps in closing the gap in initial electron conductivity between the different MTO, as formerly proposed by Senoo *et al.* [36] and Bernicke *et al.* [45]. The likely role of IrO_x NPs in electron transport was also confirmed by **Figure 3d**, where the 'specific' (*i.e.* charge-normalized) activity toward the OER of the different nanocatalysts is displayed. Indeed, the 'intrinsic' performance for the OER of IrO_x NPs was only inferior

for IrO_x/TaTO-2.5, which makes sense considering its lower Ir wt.% compared to the others TaTO aerogel supports (~11 wt.% compared to ~17-18 wt.%, see **Table 1**).

Activity-Stability Relationships for OER on IrO_x/doped SnO_2 Aerogels: Effect of the Doping Element

Accelerated Ageing Test Simulating Potential Variations at a PEMWE Anode

We then assessed the stability of the synthesized materials in 0.05 M H_2SO_4 and T = 60°C using an accelerated stress test (AST) composed of 500 potential steps between 1.20 and 1.60 V *vs.* RHE with square-wave potential ramp (3 s at each potential). This AST protocol reflects the potential range experienced by a PEMWE anode in real operating conditions [46]. As displayed in **Figure 4a, b, d** and **e**, both the intensity of the Ir(III)/Ir(IV) redox peaks and the pseudocapacitive current decreased continuously during potential cycling for the ATO-supported sample and for the commercial, unsupported IrO_2 (see **Figure S4**). In contrast, no or small changes were observed for the IrO_x/TaTO samples. These differences reflect in terms of long-term OER performance: nearly 40 % of the initial mass activity towards the OER was lost for IrO_x/ATO-10 whereas the

IrO_x/TaTO catalysts were more durable (between 70 and 90 % OER mass activity retention), even exceeding the stability of the commercial IrO_2 in case of IrO_x/TaTO-5 and IrO_x/TaTO-18 (**Figure 4c**). Moreover, a direct correlation between the mass- and the charge-normalized OER activity was noticed for IrO_x/TaTO samples, whereas these values were decoupled for IrO_x/ATO and the commercial IrO_2. These results provide clear evidence that the MTO support (and especially the doping element nature and concentration) plays a crucial role in stabilizing IrO_x NPs in the harsh anodic conditions of a PEMWE anode.

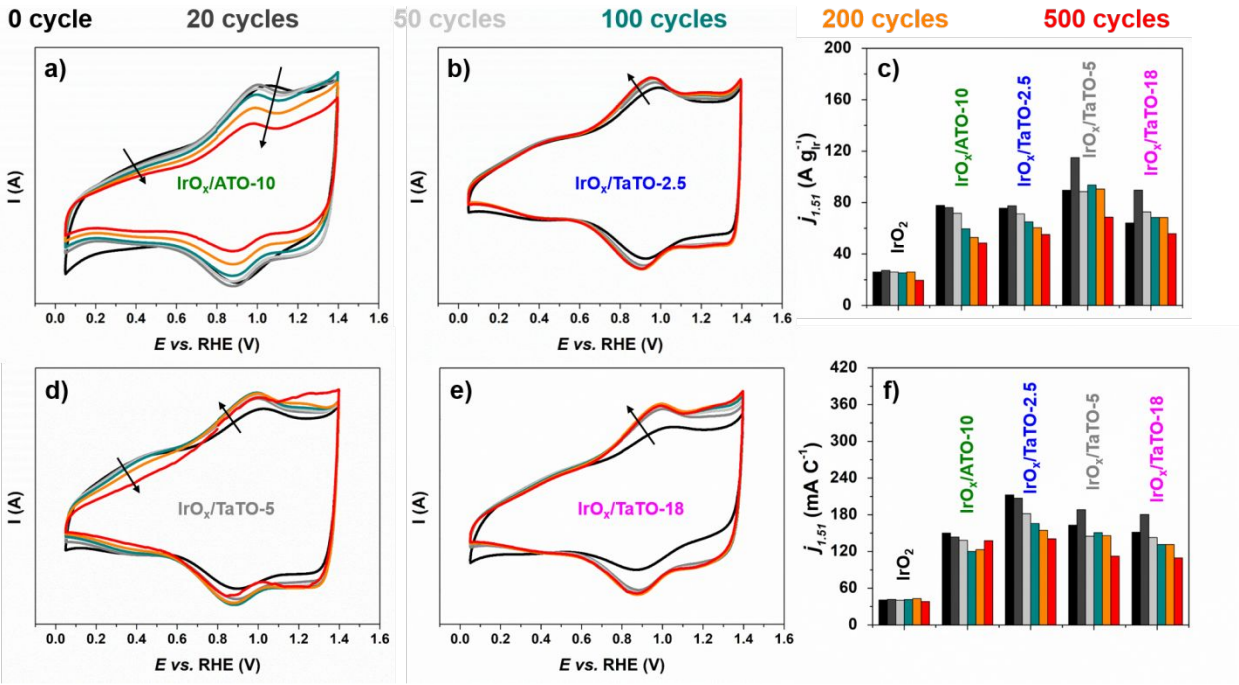

Figure 4. Changes in cyclic voltammograms and OER activity during accelerated stress testing for the various catalysts investigated in this study. Base cyclic voltammograms recorded at 50 mV s^{-1} for a) IrO_x/ATO-10, b) IrO_x/TaTO-2.5, d) IrO_x/TaTO-5 and e) IrO_x/TaTO-18 after potential stepping between 1.2 and 1.6 V *vs*. RHE with square wave ramp (3 seconds per step, T = 60°C, 0.05 M H_2SO_4). Percentage of c) the initial Ir mass-normalized OER activity at 1.51 V *vs*. RHE and f) the initial charge-normalized OER activity at 1.51 V *vs*. RHE upon cycling. The charge in f) was calculated by integration of the base voltammograms in (a, b, d and e) during the anodic potential sweep in the potential region 0.4 – 1.4 V *vs*. RHE. All OER activities were recorded in 0.05 M H_2SO_4 at T= 25 ºC at 5 mV s^{-1}.

Corrosion of Ir, Sn and Doping Elements from IrO_x/doped SnO_2 Aerogel Supports During Electrochemical Conditioning Studied by FC-ICP-MS

To analytically confirm that changes in OER activity were related to the resistance to corrosion of the doped SnO_2 supports, a home-made flow cell was connected to an ICP-MS. This set-up allowed monitoring time- and potential-dependent concentrations of Ir,

Sn and of the doping element. We first discuss the corrosion rates of IrO_x/C, IrO_x/ATO-10 and IrO_x/TaTO-5 during the electrochemical conditioning stage. For IrO_x/C (**Figure 5a**), the first potential excursion to 1.4 V *vs.* RHE led to an increase of the Ir concentration in the electrolyte, up to 10 µg L^{-1} ($t \approx 80$ s), which we ascribed to the dissolution of the IrO_x NPs (in line with former results of Cherevko *et al.* for bulk Ir [47-48]) and to their detachment from the Vulcan XC72 support. Indeed, it is well-established that high surface area carbon supports undergo severe corrosion at potential $E > 1.2$ V *vs.* RHE, even at room temperature [49-54] [55]. In the present study, such process leads to detachment of the IrO_x NPs, which are then vaporized in the plasma, and detected by the mass spectrometer. Starting from the second cycle ($t \approx 110$ s), the concentration of released Ir in the electrolyte was significantly reduced, most likely due to IrO_x and carbon surface passivation. Furthermore, Ir was detected mostly in the cathodic scan parts (*i.e.*, negative-going potential sweeps) while Ir dissolution in the anodic regions could not be clearly identified. The baseline of Ir concentration stabilized around 1 µg L^{-1} over time, *i.e.* at least one order of magnitude higher than what was observed on the other IrO_x/doped SnO_2 nanocatalysts (**Figure 5a** to **Figure 5c**). All these observations thus indicate that the

corrosion of high surface area carbon support is the dominant degradation mechanism for IrO_x/C, thereby clearly prohibiting any industrial application.

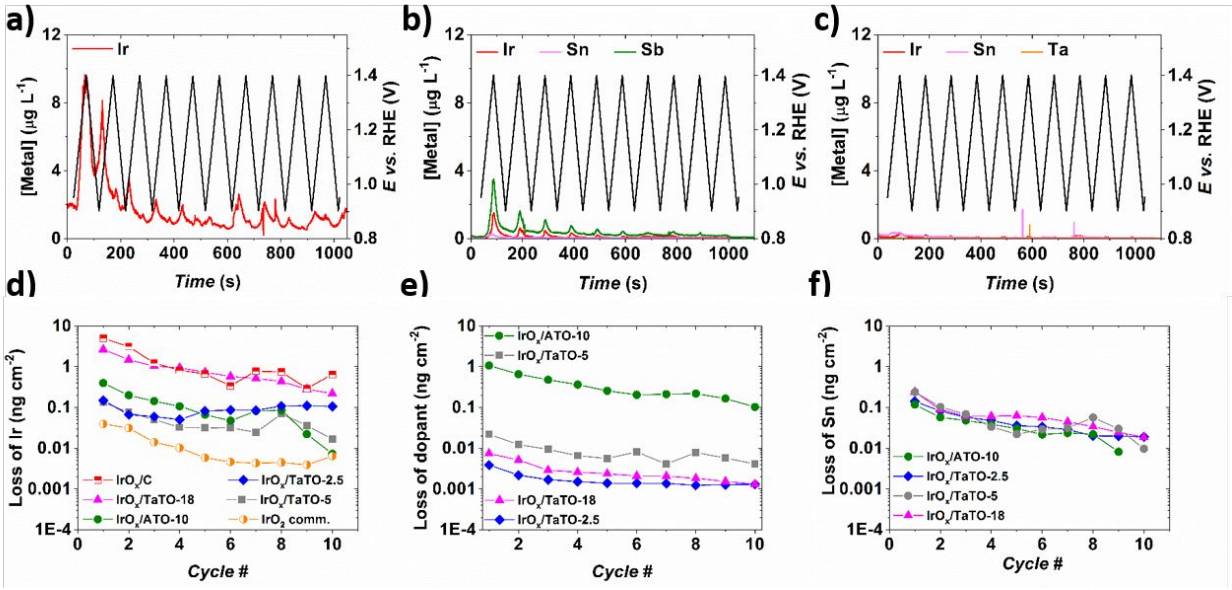

Figure 5. Time- and element-resolved materials dissolution during electrochemical conditioning. Measured corrosion of Ir, Sn and doping elements from IrO_x nanoparticles supported onto a) Vulcan XC72 support, b) ATO-10, c) TaTO-5 aerogels, and d-f) integrated signals for all synthesized nanocatalysts using FC-ICP-MS.

Figure 5b shows Ir, Sb and Sn concentration profiles for IrO_x/ATO-10 under the same potentiodynamic conditions. Compared to IrO_x/C, the Ir losses were significantly reduced; however, synchronized changes in the Sb and Ir corrosion peaks suggest that corrosion

of the ATO support also contributed to the Ir losses (**Figure 5b)**. We rationalized these results by considering the Pourbaix diagram of Sb, [56] which indicates that Sb atoms are oxidized into Sb_2O_5 in PEMWE anode operating conditions. Antimony pentoxide chemically dissolves in antimonic cations (SbO_2^+, **Equation 1**) and antimonate anions (SbO_3^-, **Equation 2**) in acidic water, and thus has a very limited stability domain.

$$Sb_2O_5 + 2\,H^+ = 2\,SbO_2^+ + H_2O \qquad \log(SbO_2^+) = -4.70 - pH \quad (1)$$

$$Sb_2O_5 + H_2O = 2\,SbO_3^- + + 2\,H^+ \qquad \log(SbO_3^-) = -4.16 + pH \quad (2)$$

Figure 5c shows changes in Ir, Ta and Sn concentration evolutions for IrO_x/TaTO-5. A slight Sn dissolution peak was noticed during the first positive going potential sweep. It was accompanied by a small, rapidly vanishing Ir dissolution peak (not synchronized with the Sn dissolution peak), which indicates that electrochemical conditioning leads to the formation of higher oxidation state Ir atoms which are more resistant towards electrochemical dissolution [30, 40-41, 57-58]. Similar results were obtained for IrO_x/TaTO-2.5, and this is most obvious from **Figure 5d** showing the Ir mass lost (ng cm^{-2}) per cycle for

all the electrocatalysts investigated in this study. Overall, the amount of dissolved doping element was *ca*. two orders of magnitude lower for the IrO_x/TaTO samples compared to IrOx/ATO-10 (**Figure 5e**). Remarkably, there was almost no effect of the dopant nature and dopant concentration on the Sn corrosion profiles (**Figure 5f**); the quantity of Sn atoms being not dependent neither on the doping element nor on its concentration in these experimental conditions (we will see later that this does not hold for experiments in harsher conditions).

Corrosion of Ir, Sn and Doping Elements from IrO_x/doped SnO_2 in OER Conditions Studied by FC-ICP-MS

To simulate the potential variations of a PEMWE anode during operation and shutdown (open circuit voltage close to 0.9 V if H_2 is not pressurized), we used an AST in which the potential was increased in a stepwise manner from 0.9 to 1.6 V *vs.* RHE (300 s at each step). **Figure 6a** shows that Ir atoms were detected in the electrolyte positive from 0.9 V *vs.* RHE on IrO_x/C. Similar to what was discussed previously, the intensity of the Ir concentration peak increased with potential reaching a maximum (*ca.* 3 ppb) at 1.6 V *vs*.

RHE as a combination of (i) Ir electrochemical dissolution and (ii) IrO_x NPs detachment from the Vulcan XC72 support. In the cathodic region (*i.e.*, for negative-going potential sweeps), two significant peaks were noticed for 0.9 V < *E* < 1.1 V *vs.* RHE. The results are in line with what was observed during the potentiodynamic test (**Figure 5a**), and suggest detachment of IrO_x NPs consecutive to reduction of the passive film that had formed on the carbon support at high potential (note that the situation is similar to what was observed on Pt/C in Refs [54, 59-60]). The Ir concentration at 1.6 V *vs.* RHE was reduced by a factor of 2 on IrO_x/ATO-10 compared to IrO_x/C. However, the loss of the Sb dopant at high potential remained an issue: indeed, we again observed that the Sb and Ir dissolution profiles were synchronized. Hence, despite claimed favourable metal-ATO support interaction on OER activity and stability, [61] our FC-ICP-MS results suggest that dissolution of Sb is the Achille's heel of ATO supports, and prevent its widespread usage in PEMWE anodes.

Figure 6c displays the Ir, Ta and Sn concentration profiles for IrO_x/TaTO-5. The Sn and Ta corrosion peaks were hardly noticeable; and Ir was detected only for *E* > 1.3 V *vs.*

RHE, in line with former observations of Cherevko et *al.* [48] for a polycrystalline Ir electrode under similar conditions. The Ir concentration peak was 2-fold less intense on IrO_x/TaTO-5 compared to IrO_x/ATO-10, and was ascribed to Ir dissolution during cyclic transition between Ir(IV)/Ir(III) oxidation states (Ir(III) is the common intermediate of the OER and of the corrosion reaction [29, 47-48, 62-65]). Similar observations were made for IrO_x/TaTO-2.5 but not for IrO_x/TaTO-10 (see **Figure S5** and **Figure S6**) and IrO_x/TATO-18, thus indicating that not only the dopant nature but also the doping concentration play an important role in the resistance to electrochemical corrosion of doped SnO_2 aerogel supports.

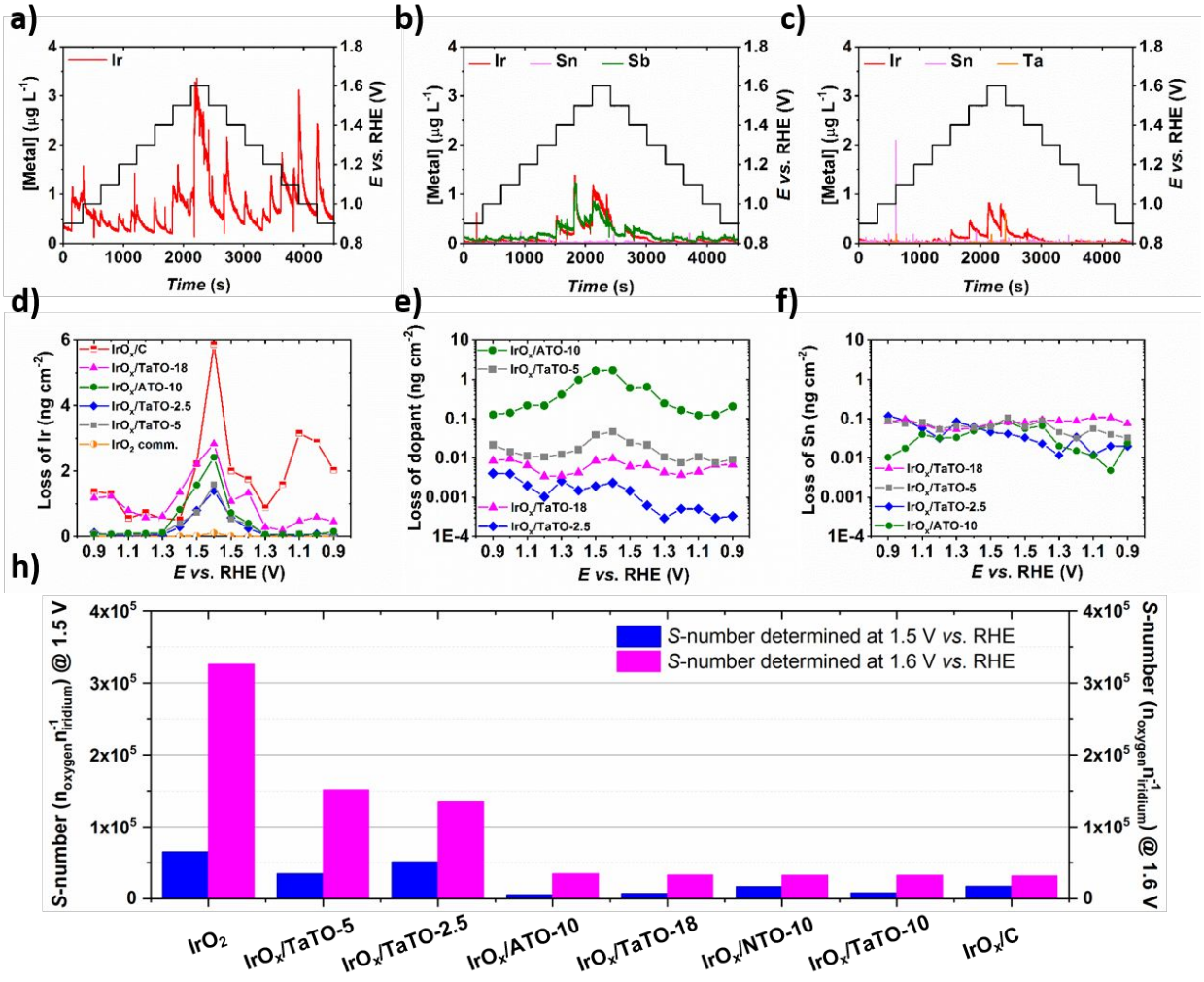

Figure 6. Time- and element- resolved materials dissolution during oxygen evolution reaction. Measured corrosion of Ir, Sn and doping elements from IrO_x nanoparticles supported onto a) high-surface area Vulcan XC72 support, b) ATO-10, c) TaTO-5. d-f) and h) represent the integrated signals and the *S*-number values calculated using FC-ICP-MS for all synthesized nanocatalysts, respectively.

We rationalized this phenomenon using XPS measurements showing that high Ta doping concentration causes reduction of the average Ir oxidation state (see **Figure S7**), which detrimentally affects the extent of Ir dissolution (see Ref. [30, 40, 47-48, 62]). To quantify the propensity of the synthesized catalysts to sustainably electrocatalyze the OER, we have plotted their *S*-number value at E = 1.5 or 1.6 V *vs*. RHE in **Figure 6h** (see calculation method in the Supporting Information). This metric, first introduced by Geiger *et al.*, [65] represents the ratio between the amounts of evolved oxygen and dissolved iridium. The determined *S*-number values approach 10^5, in line with what was found in Geiger's work (although different experimental conditions were used). These values slightly increase with the electrode potential (maybe reflecting that more stable IrO_x formed or that the less stable regions of the IrO_x/MTO catalysts dissolved first), and allow ranking the catalysts as: IrO_2 comm. >> IrO_x/TaTO-5 ≈ IrO_x/TaTO-2.5 > IrO_x/ATO-10 > IrO_x/TaTO-18 > IrO_x/NTO-10 ≈ IrO_x/TaTO-10 > IrO_x/C.

Similarities and Differences in the Resistance to Corrosion of IrO_x/doped SnO_2 Nanocatalysts: Towards a Generalized Degradation Mechanism

Following the *in situ* characterizations by FC-ICP-MS, we here discuss all the results together to draw general conclusions on the degradation mechanisms of IrO_x/doped SnO_2 nanocatalysts. By comparing the corrosion resistance of IrO_x NPs supported on Vulcan XC 72, ATO and TaTO, we first confirm that Vulcan XC72 does not meet the requirements of a PEMWE anode. Indeed, carbon support corrosion facilitates the detachment of the IrO_x NPs, resulting in high intensity Ir peak concentrations in FC-ICP-MS experiments. The adverse effects of support corrosion were clearly minored with ATO type supports, as indicated by reduced intensity of the Ir concentration peaks. However, the dissolution of Sb atoms from ATO remained a major issue, as indicated by the synchronous detection of peak concentrations of Ir and Sb. Dissolution of Sb atoms from ATO is in accordance with the Pourbaix diagram, [56] which shows that Sb atoms are chemically unstable at pH 0 and OER-relevant potentials (see **Equation 1** and **Equation 2**) cations. Keeping the same reasoning, we notice that SnO_2 is in equilibrium with stannic ions (Sn^{4+}) in acidic media (**Equation 3**):

$SnO_2 + 4\ H^+ = 2\ Sn^{4+} + 2\ H_2O$ $\log(Sn^{4+}) = -7.68 - 4\ pH$ (3)

Chemical dissolution of the SnO_2 matrix nicely accounts for the almost no dependence of the Sn dissolution profiles on the dopant nature and concentration reported in **Figure 5f** and **Figure 6f**. In contrast, Ta_2O_5 is barely soluble in solutions of sulphuric, but also hydrochloric, nitric and phosphoric acids [56, 66]. Based on these thermodynamic considerations, we therefore conclude that the stability of SnO_2 and of the doping element dictate the corrosion resistance of the different nanocatalysts. Pure SnO_2 and Sb_2O_5 materials are immediately destabilized by a dissolution equilibrium in an acidic environment, thus leading to detachment of the IrO_x NPs. In contrast, on TaTO supports, the Sn atoms are gradually dissolved but not the Ta atoms, preventing the detachment of the IrO_x NPs. To experimentally support our hypotheses, we synthesized a SnO_2 aerogel doped with Nb, an element that has similar ionic radius, and Pourbaix diagram than Ta, [67-68] and found similar resistance to corrosion in the AST conditions of **Figure 5** and **Figure 6** (see **Figure S5** and **Figure S6**). Furthermore, thanks to a dedicated microwave oven, the IrO_x/doped SnO_2 nanocatalysts were exposed to much harsher conditions, combining

higher temperature (*ca*. 225°C), pressure (up to 100 bars) and chemical environment. Because concentrated H_2SO_4 digests Nb_2O_5 and leaves Ta_2O_5 almost preserved, [67-68] *aqua regia* was used also for its highly oxidizing and complexing power both facilitating the structural transformations we suspect. The results were evaluated with ICP-MS on percentage recovery basis (ratio of the digested mass fraction of one element to that initially quantified by X-EDS and ICP-MS, see Supporting Information). We first remarked that a remaining white powder was left after digestion of the TaTO- and NTO-based samples, which corresponds to the natural colour of the doped-SnO_2 aerogel supports when no Ir is deposited (black otherwise). In contrast, no powder was left after digestion of the ATO-10 sample, thus supporting our former hypothesis that both Sn and Sb atoms chemically dissolve. In agreement with this qualitative evaluation, it is worth noting that 112 % of the initial Sn content (considering some differences between X-EDS and ICP-MS quantification results, see **Figure S7** in case of Ir wt.%) was dissolved from ATO-10 (**Figure 7a**), and that this value decreased to 53 % for TaTO-2.5, to 30-40 % for NTO-10 and TaTO-10, and to 20% or less for TaTO-5 and TaTO-18. As shown in **Figure 7b**, the stability of the doping element followed the same order, with 105 % of the initial Sb content

dissolved in case of ATO-10, around 7 % of Nb in case of NTO-10 and virtually 0 % Ta for all TaTOs supports. These findings suggest that the stability of MTO aerogels rests on the ability of the doping element to form stable near surface layers *via* either surface segregation [32-34] or enrichment of the surface and near-surface layers in doping element as a result of Sn dissolution. The second option is largely supported by our data: indeed, **Figure 7a** shows that the enrichment of the surface in Ta requires two times more dissolved Sn for TaTO-2.5 (low doping concentration) compared to TaTO-5, TaTO-10 and TaTO-18 (high doping concentration).

To further confirm this scenario, we performed STEM/X-EDS imaging on the IrO_x/TaTO-5 powder after digestion in *aqua regia*. The chemical map displayed in **Figure 7c** provides clear visual evidence that a Ta-rich shell covering the TaTO core formed during this harsh treatment. The line scan profile displayed in **Figure 7d** quantitatively shows that the doping concentration remained close to 5 at. % in the bulk but increased up to 40 at. % at the surface, thus confirming the formation of a core@shell material in which the

composition of the core was close to that of the raw material and the surface was enriched in Ta.

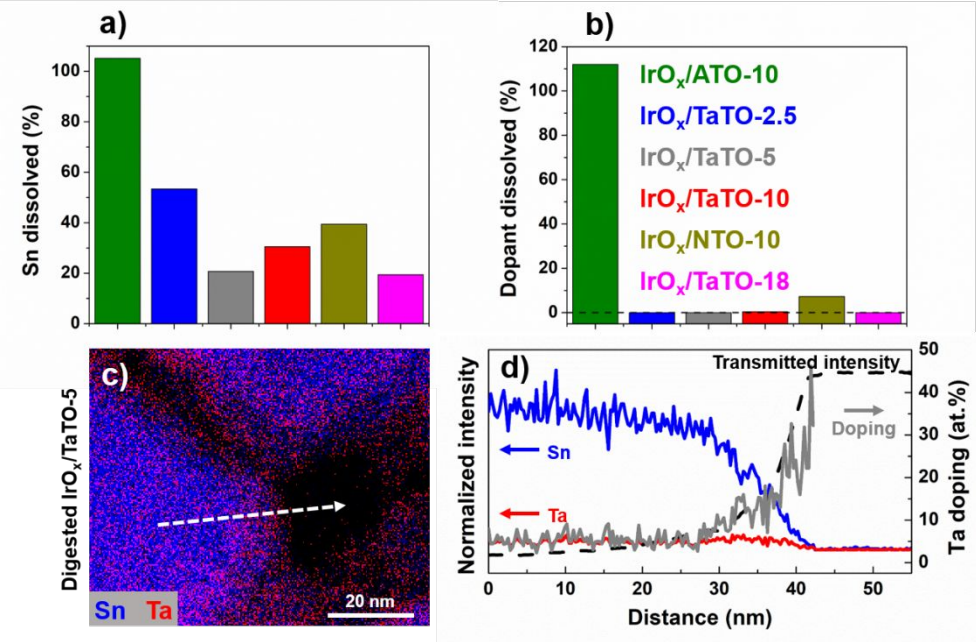

Figure 7. Quantification results of dissolved Sn, and various doping elements after microwave-assisted digestion of the IrO_x/MTO catalysts in *aqua regia*. Percentage of dissolved a) Sn and b) dopant measured by ICP-MS after digestion relative to the initial content measured by ICP-MS (Ir wt. %) and X-EDS (Sn and dopant at. %). The catalysts were heated at 225 ºC for 3 h in *aqua regia* after a 30 min. temperature ramp. The pressure was allowed to increase up to 100 bars. c) STEM/X-EDS elemental map of the IrO_x/TaTO-5 sample after digestion. Sn and Ta are displayed in blue and red,

respectively. The line scan profile in d) is measured along the white arrow displayed in c) and shows the normalized counts (*i.e.* proportional to the atomic composition) detected by X-EDS also with the spatially resolved Ta doping concentration. In d), the dashed black line represents the intensity of the transmitted beam, helping visualizing the location of the surface.

From this microwave-assisted digestion experiment in extremely harsh conditions, we therefore pointed out radical differences in materials stability. Importantly, these differences were not disclosed by the usual, rather short-term electrochemical AST procedures encountered in the field. For example, almost no difference in Sn dissolution rate during the AST was found among all the aerogel supports (**Figure 6f**), but the results of the *aqua regia* digestion experiments indicate that Sn dissolution will eventually stop for TaTO and NTO but not for ATO (**Figure 7a**). We thus propose the following guidelines to maximize the OER activity/stability of IrO_x NPs supported onto MTO supports for application at a PEMWE anode: (i) using a high Ir weight fraction to maximize the electronic conductivity of the IrO_x/doped SnO_2 nanocatalyst, (ii) doping with Ta (and in

lesser extent Nb because the latter dissolves in concentrated H_2SO_4 [66]) to ensure chemical and/or electrochemical stability of the support, (iii) fine tuning the Ta (or Nb) doping concentration *i.e.* targeting 2.5-5.0 at. %. Indeed, TaTO-2.5 features the best initial SnO_2 crystallinity and electronic conductivity but turns to be less robust than TaTO-5, TaTO-10 and TaTO-18 in OER conditions (**Figure 4f**). We rationalized this by considering that more Sn atoms need to be dissolved before the formation of the protective Ta-rich shell at low compared to high Ta doping concentrations (hence there is a higher risk of detachment of IrO_x NPs in the former case). Complementary, Ta doping concentration exceeding 5 at. % is not optimal either, in particular with respect to Ir losses (**Figure 6d** and **Figure S6b**). Several hypotheses may be proposed to account for this: (i) increasing specific surface area for the doped SnO_2 aerogels (**Table 1**), which detrimentally affects the propensity of the IrO_x NPs to detach from their support; (ii) reduction in the average Ir oxidation state (see **Figure S7**), and thus more facile Ir dissolution (see Ref. [30, 40, 47, 62]). Summing up the whole set of results, doping a SnO_2 aerogel with 5 at. % Ta represents a desirable compromise, favouring both high OER activity and long-term stability.

CONCLUSION

In this study, a sol-gel process was used to synthesized SnO_2 aerogels doped with elements that are electronically similar to the Sn^{4+} lattice species but have a different number of valence electrons, such as Sb^{5+}, Nb^{5+} and Ta^{5+} ions. A modified polyol route was then used to deposit IrO_x NPs onto the doped or undoped SnO_2 aerogels, thus ensuring a straightforward comparison of their catalytic performance towards the OER and their resistance to corrosion in acidic media. Time- and potential-dependent concentrations of Ir, Sn, Sb, Nb and Ta were established using a flow cell connected to an inductively-coupled plasma mass spectrometer. The results showed that, beyond its primary role of enhancing the support electronic conductivity, the ability of the doping element to form an electrochemically and chemically stable oxide in OER-relevant conditions determines the long-term stability of doped SnO_2 supports. The kinetics of this process and the percentage of Sn being dissolved depend on the nature and the concentration of the doping element. These fundamental insights may be used to limit the detachment of the IrO_x NPs, a degradation mechanism that was clearly underestimated in former literature reports primarily focusing on the stability of IrO_x nanoparticles in

PEMWE anode operating conditions. These results pave the way to the development of highly active and robust supported IrO_x nanocatalysts for oxygen evolution reaction in acidic media.

AUTHOR INFORMATION

Corresponding Authors

* E-mail address for F.M: frederic.maillard@lepmi.grenoble-inp.fr

Author Contributions

All authors analysed, discussed the results, drew conclusions and approved the final version of this manuscript.

γ These authors contributed equally.

CONFLICT OF INTEREST

The authors declare no competing financial interest.

ASSOCIATED CONTENT

Supporting Information.

The Supporting Information is available free of charge via the Internet at http://pubs.acs.org. It comprises:

- Materials and methods;

- Particle size distribution and TEM image of unsupported IrO_x nanoparticles;

- Scanning electron microscopy images, and associated particle size distributions for the different MTOs (M=Sb or Ta) aerogel supports;

- X-ray photoelectron spectroscopy (Ir4f level) spectra of the synthesized nanocatalysts;

- Electrochemical characterization after accelerated stress testing on the benchmark IrO_2 comm.;

- Time- and element-resolved materials dissolution during electrochemical conditioning;

- Time- and element- resolved materials dissolution during oxygen evolution reaction;

- Impact of Ta doping on the oxidation state of IrO_x nanoparticles in the as-synthesized powder or in fresh/aged catalytic suspensions.

- Comparison between Ir wt. % measured by X-EDS and ICP-MS;

ACKNOWLEDGEMENTS

This work was performed within the framework of the Centre of Excellence of Multifunctional Architectured Materials “CEMAM” (ANR-10-LABX-44-01). The French National Research Agency (MOISE project, ANR-17-CE05-0033) financially supported this research. We acknowledge Dr. Guillaume Ozouf for synthesizing and characterizing the NTO-10 aerogel and Dr. Viktor Shokhen for his kind help in designing Figure 1. F.C. acknowledges the Region Auvergne Rhône-Alpes for funding his Ph.D. thesis in the frame of the ARC Energies program (ARC 2016 n° 04 ADR).

REFERENCES

1. Millet, P., Fundamentals of Water Electrolysis. In *Hydrogen Production by Electrolysis*, Godula-Jopek, A., Ed. Wiley-VCH: Weinheim, 2015; pp 33-62.

2. Gilliam, R. J.; Graydon, J. W.; Kirk, D. W.; Thorpe, S. J., A Review of Specific Conductivities of Potassium Hydroxide Solutions for Various Concentrations and Temperatures. *Int. J. Hydrogen Energy.* **2007,** *32*, 359-364.

3. Zeng, K.; Zhang, D., Recent Progress in Alkaline Water Electrolysis for Hydrogen Production and Applications. *Prog. Energy Combust. Sci.* **2010,** *36*, 307-326.

4. Ayers, K. E.; Anderson, E. B.; Capuano, C. B.; Niedzwiecki, M.; Hickner, M. A.; Wang, C.-Y.; Leng, Y.; Zhao, W., Characterization of Anion Exchange Membrane Technology for Low Cost Electrolysis. *ECS Trans.* **2013,** *45*, 121-130.

5. Ayers, K. E.; Anderson, E. B.; Capuano, C.; Carter, B.; Dalton, L.; Hanlon, G.; Manco, J.; Niedzwiecki, M., Research Advances Towards Low Cost, High Efficiency PEM Electrolysis. *ECS Trans.* **2010,** *33*, 3-15.

6. Renner, J.; Ayers, K.; Anderson, E., Proton Exchange Membrane Electrolyzer Stack and System Design. In *PEM Electrolysis for Hydrogen Production: Principles and Applications*, Taylor & Francis: 2016.

7. Carmo, M.; Fritz, D. L.; Mergel, J.; Stolten, D., A Comprehensive Review on PEM Water Electrolysis. *Int. J. Hydrogen Energy.* **2013,** *38*, 4901-4934.

8. Bernt, M.; Siebel, A.; Gasteiger, H. A., Analysis of Voltage Losses in PEM Water Electrolyzers with Low Platinum Group Metal Loadings. *J. Electrochem. Soc.* **2018,** *165*, F305-F314.

9. Babic, U.; Suermann, M.; Büchi, F. N.; Gubler, L.; Schmidt, T. J., Critical Review—Identifying Critical Gaps for Polymer Electrolyte Water Electrolysis Development. *J. Electrochem. Soc.* **2017,** *164*, F387-F399.

10. Saba, S. M.; Müller, M.; Robinius, M.; Stolten, D., The Investment Costs of Electrolysis – a Comparison of Cost Studies from the Past 30 Years. *Int. J. Hydrogen Energy.* **2018,** *43*, 1209-1223.

11. Rozain, C.; Mayousse, E.; Guillet, N.; Millet, P., Influence of Iridium Oxide Loadings on the Performance of PEM Water Electrolysis Cells: Part II – Advanced Oxygen Electrodes. *Appl. Catal. B.* **2016,** *182*, 123-131.

12. Rozain, C.; Mayousse, E.; Guillet, N.; Millet, P., Influence of Iridium Oxide Loadings on the Performance of PEM Water Electrolysis Cells: Part I–Pure IrO_2-Based Anodes. *Appl. Catal. B.* **2016,** *182*, 153-160.

13. De Pauli, C. P.; Trasatti, S., Electrochemical Surface Characterization of IrO_2 + SnO_2 Mixed Oxide Electrocatalysts. *J. Electroanal. Chem.* **1995,** *396*, 161-168.

14. Mayousse, E.; Maillard, F.; Fouda-Onana, F.; Sicardy, O.; Guillet, N., Synthesis and Characterization of Electrocatalysts for the Oxygen Evolution in PEM Water Electrolysis. *Int. J. Hydrogen Energy.* **2011,** *36*, 10474-10481.

15. Li, G.; Yu, H.; Wang, X.; Sun, S.; Li, Y.; Shao, Z.; Yi, B., Highly Effective $Ir_xSn_{1-x}O_2$ Electrocatalysts for Oxygen Evolution Reaction in the Solid Polymer Electrolyte Water Electrolyser. *Phys. Chem. Chem. Phys.* **2013,** *15*, 2858-2866.

16. Kokoh, K. B.; Mayousse, E.; Napporn, T. W.; Servat, K.; Guillet, N.; Soyez, E.; Grosjean, A.; Rakotondrainibé, A.; Paul-Joseph, J., Efficient Multi-Metallic Anode Catalysts in a PEM Water Electrolyzer. *Int. J. Hydrogen Energy.* **2014,** *39*, 1924-1931.

17. Morimitsu, M.; Otogawa, R.; Matsunaga, M., Effects of Cathodizing on the Morphology and Composition of IrO_2-Ta_2O_5/Ti Anodes. *Electrochim. Acta.* **2000,** *46*, 401-406.

18. Lee, J.-Y.; Kang, D.-K.; Lee, K. H.; Chang, D. Y., An Investigation on the Electrochemical Characteristics of Ta_2O_5-IrO_2 Anodes for the Application of Electrolysis Process. *Mater. Sci. Appl.* **2011,** *2*, 237-243.

19. Terezo, A. J.; Bisquert, J.; Pereira, E. C.; Garcia-Belmonte, G., Separation of Transport, Charge Storage and Reaction Processes of Porous Electrocatalytic IrO_2 and IrO_2/Nb_2O_5 Electrodes. *J. Electroanal. Chem.* **2001,** *508*, 59-69.

20. Puthiyapura, V. K.; Pasupathi, S.; Su, H.; Liu, X.; Pollet, B.; Scott, K., Investigation of Supported IrO_2 as Electrocatalyst for the Oxygen Evolution Reaction in Proton Exchange Membrane Water Electrolyser. *Int. J. Hydrogen Energy.* **2014,** *39*, 1905-1913.

21. Oakton, E.; Lebedev, D.; Povia, M.; Abbott, D. F.; Fabbri, E.; Fedorov, A.; Nachtegaal, M.; Copéret, C.; Schmidt, T. J., IrO_2-TiO_2: A High-Surface-Area, Active, and Stable Electrocatalyst for the Oxygen Evolution Reaction. *ACS Catal.* **2017,** *7*, 2346-2352.

22. Chen, G.; Chen, X.; Yue, P. L., Electrochemical Behavior of Novel Ti/IrO_x-Sb_2O_5-SnO_2 Anodes. *J. Phys. Chem. B.* **2002,** *106*, 4364-4369.

23. Ardizzone, S.; Bianchi, C. L.; Cappelletti, G.; Ionita, M.; Minguzzi, A.; Rondinini, S.; Vertova, A., Composite Ternary SnO_2IrO_2-Ta_2O_5 Oxide Electrocatalysts. *J. Electroanal. Chem.* **2006,** *589*, 160-166.

24. Sasaki, K.; Takasaki, F.; Noda, Z.; Hayashi, S.; Shiratori, Y.; Ito, K., Alternative Electrocatalyst Support Materials for Polymer Electrolyte Fuel Cells. *ECS Trans.* **2010,** *33*, 473-482.

25. Nah, Y.-C.; Paramasivam, I.; Schmuki, P., Doped TiO_2 and TiO_2 Nanotubes: Synthesis and Applications. *Chemphyschem.* **2010,** *11*, 2698-2713.

26. Fabbri, E.; Habereder, A.; Waltar, K.; Kötz, R.; Schmidt, T. J., Developments and Perspectives of Oxide-Based Catalysts for the Oxygen Evolution Reaction. *Catal. Sci. Technol.* **2014,** *4*, 3800-3821.

27. Cognard, G.; Ozouf, G.; Beauger, C.; Dubau, L.; López-Haro, M.; Chatenet, M.; Maillard, F., Insights into the Stability of Pt Nanoparticles Supported on Antimony-Doped Tin Oxide in Different Potential Ranges. *Electrochim. Acta.* **2017,** *245*, 993-1004.

28. Cognard, G.; Ozouf, G.; Beauger, C.; Berthomé, G.; Riassetto, D.; Dubau, L.; Chattot, R.; Chatenet, M.; Maillard, F., Benefits and Limitations of Pt Nanoparticles Supported on Highly Porous Antimony-Doped Tin Dioxide Aerogel as Alternative Cathode Material for Proton-Exchange Membrane Fuel Cells. *Appl. Catal. B.* **2017,** *201*, 381-390.

29. Geiger, S.; Kasian, O.; Mingers, A. M.; Mayrhofer, K. J. J.; Cherevko, S., Stability Limits of Tin-Based Electrocatalyst Supports. *Sci Rep-Uk.* **2017,** *7*.

30. Claudel, F.; Dubau, L.; Berthomé, G.; Solà-Hernández, L.; Beauger, C.; Piccolo, L.; Maillard, F., Degradation Mechanisms of Oxygen Evolution Reaction Electrocatalysts: A Combined Identical-Location Transmission Electron Microscopy and X-Ray Photoelectron Spectroscopy Study. *ACS Catal.* **2019,** *9*, 4688-4698.

31. Shannon, R. D., Revised Effective Ionic Radii and Systematic Studies of Interatomic Distances in Halides and Chalcogenides. *Acta Crystallogr., Sect. A.* **1976,** *32*, 751-767.

32. Oswald, S.; Behr, G.; Dobler, D.; Werner, J.; Wetzig, K.; Arabczyk, W., Specific Properties of Fine SnO_2 Powders Connected with Surface Segregation. *Anal. Bioanal. Chem.* **2004,** *378*, 411-415.

33. Xu, C.; Tamaki, J.; Miura, N.; Yamazoe, N., Stabilization of SnO_2 Ultrafine Particles by Additives. *J. Mater. Sci.* **1992,** *27*, 963-971.

34. Szczuko, D.; Werner, J.; Oswald, S.; Behr, G.; Wetzig, K., XPS Investigations of Surface Segregation of Doping Elements in SnO_2. *Appl. Surf. Sci.* **2001,** *179*, 301-306.

35. Oakton, E.; Tillier, J.; Siddiqi, G.; Mickovic, Z.; Sereda, O.; Fedorov, A.; Copéret, C., Structural Differences between Sb- and Nb-Doped Tin Oxides and Consequences for Electrical Conductivity. *New J. Chem.* **2016,** *40*, 2655-2660.

36. Senoo, Y.; Kakinuma, K.; Uchida, M.; Uchida, H.; Deki, S.; Watanabe, M., Improvements in Electrical and Electrochemical Properties of Nb-Doped $SnO_{2-\delta}$ Supports for Fuel Cell Cathodes Due to Aggregation and Pt Loading. *RSC Adv.* **2014,** *4*, 32180-32188.

37. Cognard, G.; Ozouf, G.; Beauger, C.; Jiménez-Morales, I.; Cavaliere, S.; Jones, D.; Rozière, J.; Chatenet, M.; Maillard, F., Pt Nanoparticles Supported on Niobium-Doped Tin Dioxide: Impact of the Support Morphology on Pt Utilization and Electrocatalytic Activity. *Electrocatalysis.* **2017,** *8*, 51-58.

38. Hartig-Weiss, A.; Miller, M.; Beyer, H.; Schmitt, A.; Siebel, A.; Freiberg, A. T. S.; Gasteiger, H. A.; El-Sayed, H. A., Iridium Oxide Catalyst Supported on Antimony-Doped Tin Oxide for High Oxygen Evolution Reaction Activity in Acidic Media. *ACS Appl. Nano Mater.* **2020,** *3*, 2185-2196.

39. Kuo, D.-Y.; Kawasaki, J. K.; Nelson, J. N.; Kloppenburg, J.; Hautier, G.; Shen, K. M.; Schlom, D. G.; Suntivich, J., Influence of Surface Adsorption on the Oxygen Evolution Reaction on IrO_2(110). *J. Am. Chem. Soc.* **2017,** *139*, 3473-3479.

40. Scohy, M.; Abbou, S.; Martin, V.; Gilles, B.; Sibert, E.; Dubau, L.; Maillard, F., Probing Surface Oxide Formation and Dissolution on/of Ir Single Crystals via X-Ray Photoelectron Spectroscopy and Inductively Coupled Plasma Mass Spectrometry. *ACS Catal.* **2019,** *9*, 9859-9869.

41. Lettenmeier, P.; Majchel, J.; Wang, L.; Saveleva, V. A.; Zafeiratos, S.; Savinova, E. R.; Gallet, J. J.; Bournel, F.; Gago, A. S.; Friedrich, K. A., Highly Active Nano-Sized Iridium Catalysts: Synthesis and *Operando* Spectroscopy in a Proton Exchange Membrane Electrolyzer. *Chem. Sci.* **2018,** *9*, 3570-3579.

42. Alia, S. M.; Anderson, G. C., Iridium Oxygen Evolution Activity and Durability Baselines in Rotating Disk Electrode Half-Cells. *J. Electrochem. Soc.* **2019,** *166*, F282-F294.

43. Böhm, D.; Beetz, M.; Schuster, M.; Peters, K.; Hufnagel, A. G.; Döblinger, M.; Böller, B.; Bein, T.; Fattakhova-Rohlfing, D., Efficient OER Catalyst with Low Ir Volume Density Obtained by Homogeneous Deposition of Iridium Oxide Nanoparticles on Macroporous Antimony-Doped Tin Oxide Support. *Adv. Funct. Mater. 0*, 1906670.

44. Solà-Hernández, L.; Claudel, F.; Maillard, F.; Beauger, C., Doped Tin Oxide Aerogels as Oxygen Evolution Reaction Catalyst Supports. *Int. J. Hydrogen Energy.* **2019,** *44*, 24331-24341.

45. Bernicke, M.; Bernsmeier, D.; Paul, B.; Schmack, R.; Bergmann, A.; Strasser, P.; Ortel, E.; Kraehnert, R., Tailored Mesoporous Ir/TiO_x: Identification of Structure-Activity Relationships for an Efficient Oxygen Evolution Reaction. *J. Catal.* **2019,** *376*, 209-218.

46. Weiß, A.; Siebel, A.; Bernt, M.; Shen, T.-H.; Tileli, V.; Gasteiger, H. A., Impact of Intermittent Operation on Lifetime and Performance of a PEM Water Electrolyzer. *J. Electrochem. Soc.* **2019,** *166*, F487-F497.

47. Cherevko, S.; Geiger, S.; Kasian, O.; Mingers, A.; Mayrhofer, K. J. J., Oxygen Evolution Activity and Stability of Iridium in Acidic Media. Part 2. – Electrochemically Grown Hydrous Iridium Oxide. *J. Electroanal. Chem.* **2016,** *774*, 102-110.

48. Cherevko, S.; Geiger, S.; Kasian, O.; Mingers, A.; Mayrhofer, K. J. J., Oxygen Evolution Activity and Stability of Iridium in Acidic Media. Part 1. – Metallic Iridium. *J. Electroanal. Chem.* **2016,** *773*, 69-78.

49. Maass, S.; Finsterwalder, F.; Frank, G.; Hartmann, R.; Merten, C., Carbon Support Oxidation in PEM Fuel Cell Cathodes. *J. Power Sources.* **2008,** *176*, 444-451.

50. Liu, Z. Y.; Zhang, J. L.; Yu, P. T.; Zhang, J. X.; Makharia, R.; More, K. L.; Stach, E. A., Transmission Electron Microscopy Observation of Corrosion Behaviors of Platinized Carbon Blacks under Thermal and Electrochemical Conditions. *J. Electrochem. Soc.* **2010,** *157*, B906-B913.

51. Castanheira, L.; Dubau, L.; Maillard, F., Accelerated Stress Tests of Pt/HSAC Electrocatalysts: An Identical-Location Transmission Electron Microscopy Study on the Influence of Intermediate Characterizations. *Electrocatalysis.* **2014,** *5*, 125-135.

52. Castanheira, L.; Dubau, L.; Mermoux, M.; Berthomé, G.; Caqué, N.; Rossinot, E.; Chatenet, M.; Maillard, F., Carbon Corrosion in Proton-Exchange Membrane Fuel Cells: From Model Experiments to Real-Life Operation in Membrane Electrode Assemblies. *ACS Catal.* **2014,** *4*, 2258-2267.

53. Dubau, L.; Castanheira, L.; Chatenet, M.; Maillard, F.; Dillet, J.; Maranzana, G.; Abbou, S.; Lottin, O.; De Moor, G.; El Kaddouri, A.; Bas, C.; Flandin, L.; Rossinot, E.; Caqué, N., Carbon Corrosion Induced by Membrane Failure: The Weak Link of PEMFC Long-Term Performance. *Int. J. Hydrogen Energy.* **2014,** *39*, 21902–21914.

54. Castanheira, L.; Silva, W. O.; Lima, F. H. B.; Crisci, A.; Dubau, L.; Maillard, F., Carbon Corrosion in Proton-Exchange Membrane Fuel Cells: Effect of the Carbon Structure, the Degradation Protocol, and the Gas Atmosphere. *ACS Catal.* **2015,** *5*, 2184-2194.

55. Geiger, S. Stability Investigations of Iridium-Based Catalysts Towards Acidic Water Splitting. Ruhr-Universität Bochum, Düsseldorf, 2018.

56. Pourbaix, M., *Atlas of Electrochemical Equilibria in Aqueous Solutions*. Pergamon: 1966; Vol. 1.

57. Li, T.; Kasian, O.; Cherevko, S.; Zhang, S.; Geiger, S.; Scheu, C.; Felfer, P.; Raabe, D.; Gault, B.; Mayrhofer, K. J. J., Atomic-Scale Insights into Surface Species of Electrocatalysts in Three Dimensions. *Nat. Catal.* **2018,** *1*, 300-305.

58. Scohy, M.; Montella, C.; Claudel, F.; Abbou, S.; Dubau, L.; Maillard, F.; Sibert, E.; Sunde, S., Investigating the Oxygen Evolution Reaction on Ir(111) Electrode in Acidic Medium Using Conventional and Dynamic Electrochemical Impedance Spectroscopy. *Electrochim. Acta.* **2019,** *320*.

59. Willsau, J.; Heitbaum, J., The Influence of Pt-Activation on the Corrosion of Carbon in Gas Diffusion Electrodes—a DEMS Study. *J. Electroanal. Chem. Interfacial Electrochem.* **1984,** *161*, 93-101.

60. Maillard, F.; O. Silva, W.; Castanheira, L.; Dubau, L.; Lima, F. H. B., Carbon Corrosion in Proton-Exchange Membrane Fuel Cells: Spectrometric Evidence for Pt-Catalysed Decarboxylation at Anode-Relevant Potentials. *Chemphyschem.* **2019,** *30*, 3106-3111.

61. Oh, H. S.; Nong, H. N.; Reier, T.; Bergmann, A.; Gliech, M.; Ferreira De Araújo, J.; Willinger, E.; Schlögl, R.; Teschner, D.; Strasser, P., Electrochemical Catalyst-Support

Effects and Their Stabilizing Role for IrO_x Nanoparticle Catalysts During the Oxygen Evolution Reaction. *J. Am. Chem. Soc.* **2016,** *138*, 12552-12563.

62. Kasian, O.; Grote, J. P.; Geiger, S.; Cherevko, S.; Mayrhofer, K. J. J., The Common Intermediates of Oxygen Evolution and Dissolution Reactions During Water Electrolysis on Iridium. *Angew. Chem., Int. Ed. Engl.* **2018,** *57*, 2488-2491.

63. Jovanovic, P.; Hodnik, N.; Ruiz-Zepeda, F.; Arcon, I.; Jozinovic, B.; Zorko, M.; Bele, M.; Sala, M.; Selih, V. S.; Hocevar, S.; Gaberscek, M., Electrochemical Dissolution of Iridium and Iridium Oxide Particles in Acidic Media: Transmission Electron Microscopy, Electrochemical Flow Cell Coupled to Inductively Coupled Plasma Mass Spectrometry, and X-Ray Absorption Spectroscopy Study. *J Am Chem Soc.* **2017,** *139*, 12837-12846.

64. Spori, C.; Kwan, J. T. H.; Bonakdarpour, A.; Wilkinson, D. P.; Strasser, P., The Stability Challenges of Oxygen Evolving Catalysts: Towards a Common Fundamental Understanding and Mitigation of Catalyst Degradation. *Angew Chem Int Ed Engl.* **2017,** *56*, 5994-6021.

65. Geiger, S.; Kasian, O.; Ledendecker, M.; Pizzutilo, E.; Mingers, A. M.; Fu, W. T.; Diaz-Morales, O.; Li, Z.; Oellers, T.; Fruchter, L.; Ludwig, A.; Mayrhofer, K. J. J.; Koper,

M. T. M.; Cherevko, S., The Stability Number as a Metric for Electrocatalyst Stability Benchmarking. *Nat. Catal.* **2018,** *1*, 508-515.

66. Agulyansky, A., *Chemistry of Tantalum and Niobium Fluoride Compounds*. Elsevier Science: Amsterdam, 2004; p 1-396.

67. Lambert, J. B., Tantalum and Tantalum Compounds. In *Kirk-Othmer Encyclopedia of Chemical Technology*, 2001.

68. Schlewitz, J. E., Niobium and Niobium Compounds. In *Kirk-Othmer Encyclopedia of Chemical Technology*, 2009; pp 1-27.

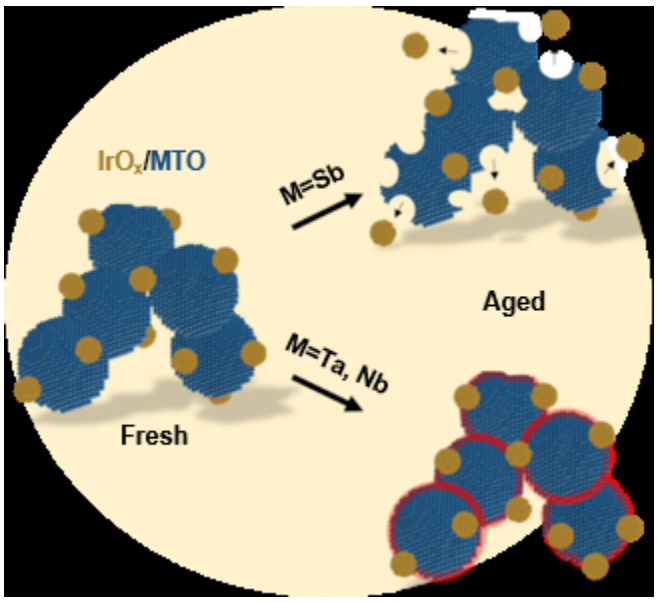

Self-Healing Metal Oxides: The nature and the concentration of the doping element of SnO_2 aerogel supports control their resistance to corrosion.

55x49mm (150 x 150 DPI)